Available online at www.sciencedirect.com
ScienceDirect
Trans. Nonferrous Met. Soc. China 34(2024) 504−518
Transactions of Nonferrous Metals Society of China
www.tnmsc.cn

Ductility enhancement by activating non-basal slip in Mg alloys with micro-Mn

Shi-bo ZHOU[1,2], Ting-ting LIU[3], Ai-tao TANG[1,4], Hui SHI[2], Xue-rui JING[1], Peng PENG[5], Jian-yue ZHANG[6], Fu-sheng PAN[1,4]

1. College of Materials Science and Engineering, Chongqing University, Chongqing 400044, China;
2. Institute of Metallic Biomaterials, Helmholtz-Zentrum Hereon, Max-Planck-Straße 1, D-21502, Geesthacht, Germany;
3. School of Materials and Energy, Southwest University, Chongqing 400715, China;
4. National Engineering Research Center for Magnesium Alloys, Chongqing University, Chongqing 400044, China;
5. School of Metallurgy and Materials Engineering, Chongqing University of Science and Technology, Chongqing 401331, China;
6. Department of Materials Science and Engineering, The Ohio State University, Columbus, OH 43210, USA

Received 4 August 2022; accepted 20 March 2023

Abstract: The effect of micro-Mn addition on the microstructure and mechanical properties of Mg alloys was analyzed. Electron back scattered diffraction, slip traces analysis, transmission electron microscopy and visco-plastic self-consistent polycrystal constitutive modeling were performed to investigate the deformation mechanisms in the tensile test. The results show that the average grain size of Mg−Mn alloys decreases from 28.30 to 5.10 μm with Mn addition. Furthermore, with the increment of Mn content, the ductility of the as-extruded samples improves from 14.33% to 20.33%, and the yield strength increases from 84 to 180 MPa. The reason for this simultaneous improvement is that the critical resolved shear stress gap between basal slip and non-basal slip decreases from 173 to 115 MPa, which leads to the increase of non-basal slip activity. The adjustment of slip system difference by microalloying elements provides a way to develop Mg alloys with high strength and ductility.

Key words: Mg alloy; microstructure evolution; mechanical properties; ductility; deformation mechanisms

1 Introduction

Magnesium (Mg) and its alloys are excellent candidates for structural materials because of their low density, high specific strength, good electromagnetic shielding performance, and other advantages [1−4]. However, the large-scale application of Mg alloys in industries is limited by their poor formability at room temperature (RT) due to the unique crystal structure (hexagonal close-packed structure (hcp)) of Mg [5−7]. The hcp structure only provides two separate slip systems to participate in plastic deformation at room temperature, which does not satisfy the Von-Mises and Taylor criterion at RT [8,9]. Therefore, more slip needs to be introduced to coordinate the *c*-axis for plastic deformation at RT. Furthermore, the activation of non-basal slip (prismatic and pyramidal slip) is known to be more difficult than that of basal slip. According to previous reports [10−12], the critical resolved shear stress (CRSS) of pyramidal ⟨*c*+*a*⟩ slip is two orders of magnitude larger than that of basal ⟨*a*⟩ slip in pure

Corresponding author: Ting-ting LIU, Tel: +86-13594630668, E-mail: ttliu@swu.edu.cn;
Ai-tao TANG, Tel: +86-23-65106121, E-mail: tat@cqu.edu.cn
DOI: 10.1016/S1003-6326(23)66413-1

Mg. Therefore, basal slip is easy to be activated at RT and plays a dominant role in plastic deformation, leading to poor ductility.

Over the past few decades, an increasing number of researchers have concentrated on improving the mechanical properties of Mg alloys by alloying [13−15], texture weakening [16,17], twining [18,19], and grain refining [20,21], etc. Alloying is one of the most effective methods to improve yield strength and maintain ductility in Mg alloys. And recently, it has been reported that the alloying element can reduce the critical resolved shear stress gap between non-basal and basal slip, activating more non-basal slip to accommodate the strain along the *c*-axis. SANDLÖBES et al [22] reported that Mg−Y alloys are substantially more ductile than pure Mg because the Y element induces more non-basal slip to participate in plastic deformation. YANG et al [8] used a modified lattice rotation method to demonstrate that the high ductility of Mg−Gd alloys is due to the addition of Gd, which increases non-basal slip and cross-slip. In addition, WU et al [23] showed that element Y could increase the $\langle c+a \rangle$ cross-slip, and they established a quantitative theory for obtaining Mg alloys with high ductility.

However, the addition of RE elements increases the cost, which limits the application of automotive manufacturing. Therefore, RE-free Mg alloys with excellent mechanical properties have been developed. For example, ZHU et al [24] reported that the Ca element increases the activity of non-basal slip and decreases the stacking fault energy (γ_{us}) for all slip modes in Mg, thus increasing the ductility. Moreover, ZENG et al [25] pointed out that Ca and Zn elements can enhance ductility due to texture and grain refinement weakening caused by Ca segregation around the grain boundary. Therefore, adding RE-free elements is also a good way to improve plasticity.

In addition, Mg−Mn-based alloys are the current research hotspot, and some progress has been achieved in the development of Mg alloys with high ductility. Most investigations have focused on the effects of Mn on microstructure evolution and mechanical properties [26,27]. YU et al [28] found that Mg−1wt.%Mn alloy had more excellent elongation and strength than pure Mg because the ultra-fined microstructure decreased the critical resolved shear stress (CRSS) and increased the activity of prismatic slip. Additionally, YU et al [26] also certificated that a high content of Mn can improve the mechanical properties, which is attributed to the fact that high-density nanoscale Mn precipitates can refine the microstructure and weaken the basal texture. Similarly, SOMEKAWA et al [29] pointed out that Mn can improve the ductility of Mg alloys by enhancing grain boundary sliding at room temperature. Furthermore, the addition of Mn can significantly improve the yield strength. PENG et al [30] found that the trace amount of Mn can effectively enhance the yield and ultimate tensile strength by forming the bimodal grain structure. The effect of Mn is mainly focused on the mechanical properties and microstructure, although the deformation mechanism has yet to be well known.

In this work, four Mg−*x*Mn (*x*=0, 0.3, 0.6, and 0.9 wt.%) binary alloys were produced to further understand the deformation mechanism of Mg−Mn binary alloys. Furthermore, the electron back-scattered diffraction (EBSD), transmission electron microscope (TEM), EBSD-assisted slip traces analysis, and visco-plastic self-consistent (VPSC) were applied to investigating the effect of micro-Mn on microstructure evolution, work-hardening behavior, and plastic deformation for Mg alloys. Furthermore, the current conclusion and discussion can provide theoretical support for the design, development, and application of Mg alloys.

2 Experimental

2.1 Experiment procedure

In the present work, Mg−*x*Mn (*x*=0, 0.3, 0.6, and 0.9 wt.%) alloys were produced by high pure Mg (99.99 wt.%) and Mg−3wt.%Mn master alloys, and the experimental samples were prepared by the traditional casting method. Firstly, pure Mg and Mg−Mn master alloys were melted in an electrical furnace with a protective atmosphere of SF_6 and CO_2 (V_{SF_6}:V_{CO_2}=1:99). Secondly, the melt was stirred and held at 720 °C for 30 min to ensure that the melt was mixed well. Finally, the ingots were obtained by cooling the iron crucible in hot salt water at about 60 °C. The ingot was machined to a diameter of 80 mm and a height of 100 mm. The actual composition of as-cast Mg−*x*Mn alloys was analyzed by X-ray fluorescence spectrometry (XRF), and their corresponding results are listed in

Table 1. The ingots were covered with graphite and were solid solution treated at 550 °C for 24 h. Then, the ingots were extruded into *d*16 mm bars using a horizontal extruder with a rated speed of 3 m/min and an extrusion ratio of 25:1 at 350 °C.

Table 1 Chemical compositions of as-cast Mg−*x*Mn alloys (wt.%)

Alloy	Mn	Mg
Pure Mg	0	Bal.
Mg−0.3Mn	0.32	Bal.
Mg−0.6Mn	0.64	Bal.
Mg−0.9Mn	0.91	Bal.

The second phase identification was carried out by the X-ray diffractometer (XRD, D/Max 2500 PC) with Cu K_α at the voltage of 40 kV and current of 200 mA. The microstructure observation of Mg−*x*Mn samples was used by scanning electron microscopy (SEM, JEOL JSM−7800F) with an energy dispersive X-ray spectrometer (EDS) detector, electron backscattered diffraction (EBSD, JSM−7800F-NordlysMax2) and transmission electron microscope (TECNAI G2 F20). The EBSD samples were prepared by metallurgical polishing and electro-polishing in an AC2 electrolyte at −20 °C. And the results were analyzed by HKL-Channel 5 software. The TEM samples were first metallurgically polished to 80 μm and then ion thinning to <100 nm. The TEM data were analyzed by Digital Micrograph software. It is noted that the sample observation direction is perpendicular to the extrusion direction.

Nanoindentation experiments were performed using a three-sided Berkovich diamond on a nanoindenter (Agilent Technologies G200). The tensile test was performed to analyze the mechanical properties of Mg−*x*Mn alloys. The specimens for the tensile test were machined from the as-extruded rods with a gauge length of 25 mm, a width of 6 mm, and a thickness of 3 mm. The tensile test was conducted on the CMT6305−300kN testing machine at room temperature with 1.5 mm/min. In addition, three samples were evaluated to obtain accurate values.

The activation of several slip systems was revealed by EBSD-assisted slip traces analysis. The Euler angle and all possible slip systems were obtained by EBSD and SEM analysis and acted as inputs to evaluate the ideal slip traces based on the MATLAB software and MTEX code [31]. It is worth noting that the strain for each experimental sample was 50% to ensure enough slip traces for each sample and compare these results. In addition, each EBSD result needs at least 100 grains to provide accurate statistics.

2.2 Computational simulation

The crystal plasticity model was used to predict and understand the tensile deformation mechanism of as-extruded Mg−*x*Mn alloys. Hence, the computer program VPSC was applied to simulating the polycrystalline aggregate plastic deformation. In addition, the visco-plastic constitutive behavior at the local level was based on the non-linear rate-sensitivity equation [32,33]:

$$\varepsilon_{ij}(\bar{x})=\sum_{s} m_{ij}^{s}\gamma^{s}(\bar{x})=\gamma_0\sum_{s} m_{ij}^{s}\left(\frac{m_{kl}^{s}\sigma_{kl}(\bar{x})}{\tau_0^{s}}\right)^{n} \quad (1)$$

where τ^s and $m_{ij}^{s}\left(=\frac{1}{2}\left(\frac{m_{kl}^{s}\sigma_{kl}(\bar{x})}{\tau_0^{s}}\right)\right)$ are the threshold stress and the Schmid tensor associated with the slip system, respectively; $\varepsilon_{ij}(\bar{x})$ and $\sigma_{kl}(\bar{x})$ are the deviatoric strain rate and stress, respectively; $\gamma^{s}(\bar{x})$ is the local shear rate on slip system; m_{kl}^{s} is the viscoplastic compliance; γ_0 is a normalization factor; n is the rate sensitivity exponent.

The threshold stress τ^s is a measurement of the resistance to activation that deformation modes encounter on an average basis. Typically, the value rises with deformation. It is characterized by the Voce law [34,35]:

$$\hat{\tau}^{s}=\tau_0^{s}+(\tau_1^{s}+\theta_1^{s}\Gamma)\left[1-\exp\left(-\Gamma\left|\theta_0^{s}/\tau_1^{s}\right|\right)\right] \quad (2)$$

Aforementioned $\Gamma=\sum\Delta\gamma^{s}$ is denoted as the accumulated shear in the grain. τ_0, θ_0 and θ_1 are the initial CRSS, the initial hardening rate, the asymptotic hardening rate, and the back extrapolated CRSS, respectively. In this work, 1000 Euler angles data and fractions for each sample were selected for simulation.

3 Results

3.1 Phase composition

The phase diagram of Mg−Mn alloys and XRD patterns of the as-solid solution Mg−*x*Mn alloys are illustrated in Fig. 1. The result of the

thermodynamic equilibrium shows that there are two phases in the Mg-rich corner, α-Mg and α-Mn phase. Meanwhile, the red dot lines in Fig. 1(a) exhibit that 0.9 wt.% Mn is completely dissolved in the Mg matrix at 550 °C. Similarly, only α-Mg phase was identified in XRD patterns (Fig. 1(b)) of the Mg−xMn alloys prepared in this work, which exhibit the same diffraction peak as pure Mg. As demonstrated in Fig. 2, SEM and EDS findings of as-solid solution Mg−0.9wt.%Mn also indicate that Mn dissolved in the Mg matrix.

3.2 Mechanical properties and fracture morphology

The mechanical properties evolution of as-extruded Mg−xMn alloys are presented in Fig. 3(a). The corresponding tensile yield strength (TYS), ultimate tensile strength (UTS), and failure elongation (FE) are illustrated in Table 2. The TYS, UTS and FE are significantly improved compared

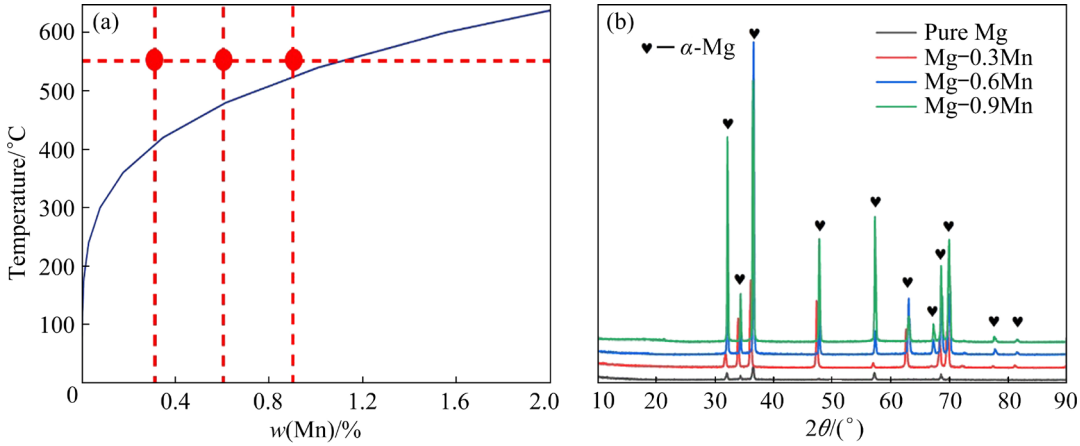

Fig. 1 Phase diagram of Mg−Mn alloys (a), and XRD patterns of as-solid solution Mg−xMn alloys (b)

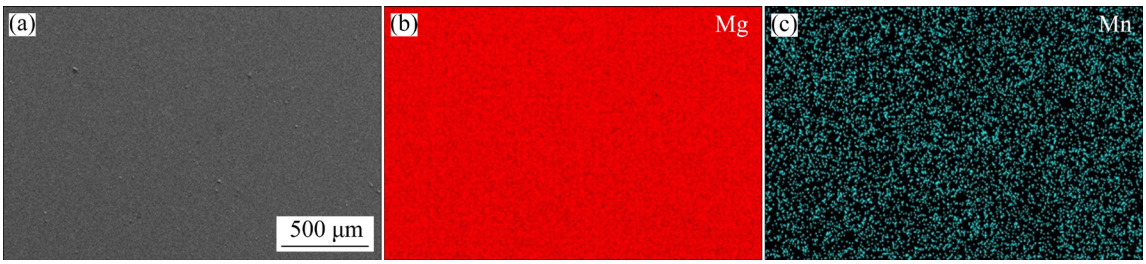

Fig. 2 SEM image (a) and EDS maps (b, c) of Mg−0.9Mn alloy

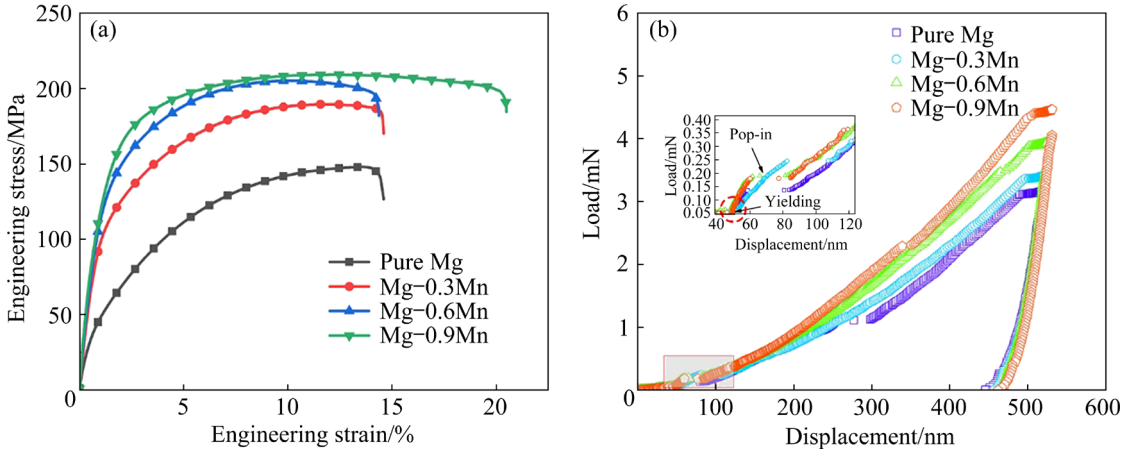

Fig. 3 Effect of Mn content on mechanical properties of as-extruded Mg−xMn alloys in tensile testing along extrusion: (a) Engineering tensile stress−strain curves; (b) Typical nanoindentation load−displacement curves, showing yielding and pop-in behavior

Table 2 TYS, UTS and FE of Mg−*x*Mn alloys

Alloy	TYS/MPa	UTS/MPa	FE/%
Pure Mg	84	146	14.33
Mg−0.3Mn	140	188	14.36
Mg−0.6Mn	162	204	14.22
Mg−0.9Mn	180	209	20.31

with pure Mg. Especially with the addition of Mn to 0.9 wt.%, the TYS increases from 84 to 180 MPa, the UTS increases from 146 to 209 MPa, and the FE increases from 14.33% to 20.31%. That is, the TYS of Mg−0.9Mn alloy increases by 114%, and the ductility increases by 42%. Figure 3(b) shows the typical nanoindentation load−displacement curves of Mg−*x*Mn alloys. Within the load range, the load of all the alloys increases significantly with the increase of the strain ($\dot{\varepsilon}_L$) at an indenter displacement of 520 nm. Notably, the gradual yielding phenomenon can be seen in all four alloys. The pop-in behavior (as shown by the black arrowed) was also detected in experiments when the applied load range was 0.1−0.3 mN. These results reveal that the deformation mechanism of Mg−*x*Mn alloys has been changed, and there is no longer only basal slip, for instance, but also twin and non-basal slip. Similarly, this result is consistent with that of GUO et al [36,37]. The possible mechanism will be explored in the following Section 4.

The SEM fracture morphology of as-extruded Mg−*x*Mn alloys is displayed in Fig. 4. It is clearly seen that the tensile fracture surface has changed from brittle fracture to ductile fracture from Figs. 4(a−d). In Fig. 4(a_1), it is found that the fracture of pure Mg exhibits a classical brittle fracture with a large number of cleavage planes and tearing ridges. With the Mn addition (Fig. 4(b_1)), the fracture morphology does not change significantly. However, when the Mn content increases to 0.9 wt.% (Fig. 4(d_1)), the fracture morphology changes clearly, and many dimples appear although there are a few tearing edges. In a word, the fracture of as-extruded Mg−*x*Mn alloys is composed of cleavage planes, tearing ridges, and dimples.

3.3 Microstructure evolution

The EBSD micrographs, grain size distribution, pole figure, and in-grain misorientation axes (IGMA) maps of as-extruded Mg−*x*Mn alloys are illustrated in Fig. 5. From the results of Figs. 4(a−d), the IPF maps show that all the samples exhibit the relatively complete dynamic recrystallized (DRXed) grain structure. According to the results of EBSD micrographs, the grain orientation of all alloys is mainly $(01\bar{1}0)$ and $(\bar{1}2\bar{1}0)$, which indicates that the addition of Mn does not change the orientation of pure Mg. Notably, the DRXed grains of all samples exhibit uniform sizes. However, some DRXed grains of Mg−0.9Mn alloy have inhomogeneity grain size after hot extrusion. On the other hand, the average grain size (AGS) reduces dramatically from 28.30 to 5.10 μm with Mn content increasing from 0 to 0.9 wt.% (Figs. 5(a_1) to (d_1)). Additionally, the pole figure results show that all the alloys exhibit the characteristic fiber texture. And the texture intensity increases from 9.79 to 15.30 with Mn addition. When the Mn content increases to 0.9 wt.%, the texture intensity slightly decreases from 15.30 to 14.73. At the same time,

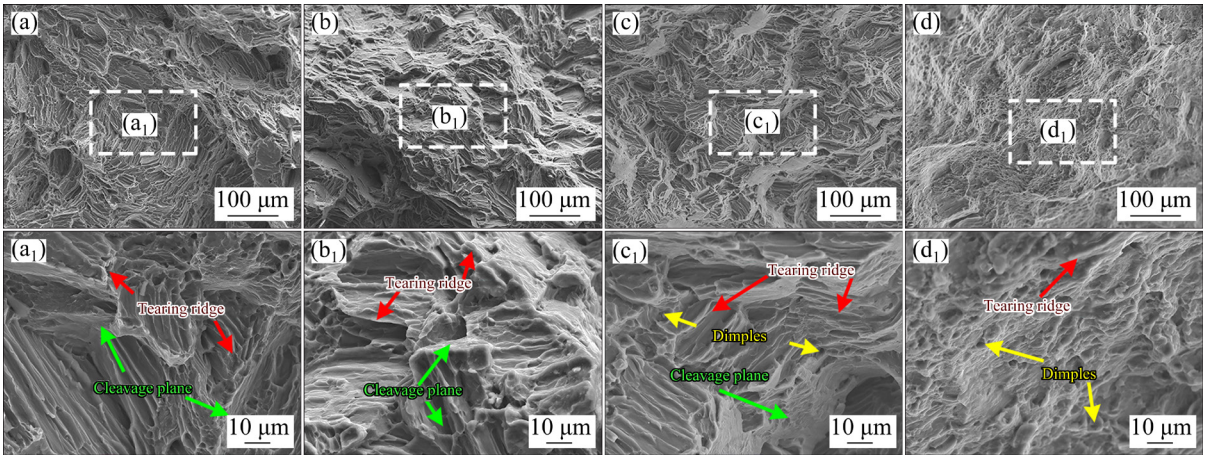

Fig. 4 SEM fracture morphology of as-extruded Mg−*x*Mn alloys: (a, a_1) Pure Mg; (b, b_1) Mg−0.3Mn alloy; (c, c_1) Mg−0.6Mn alloy; (d, d_1) Mg−0.9Mn alloy

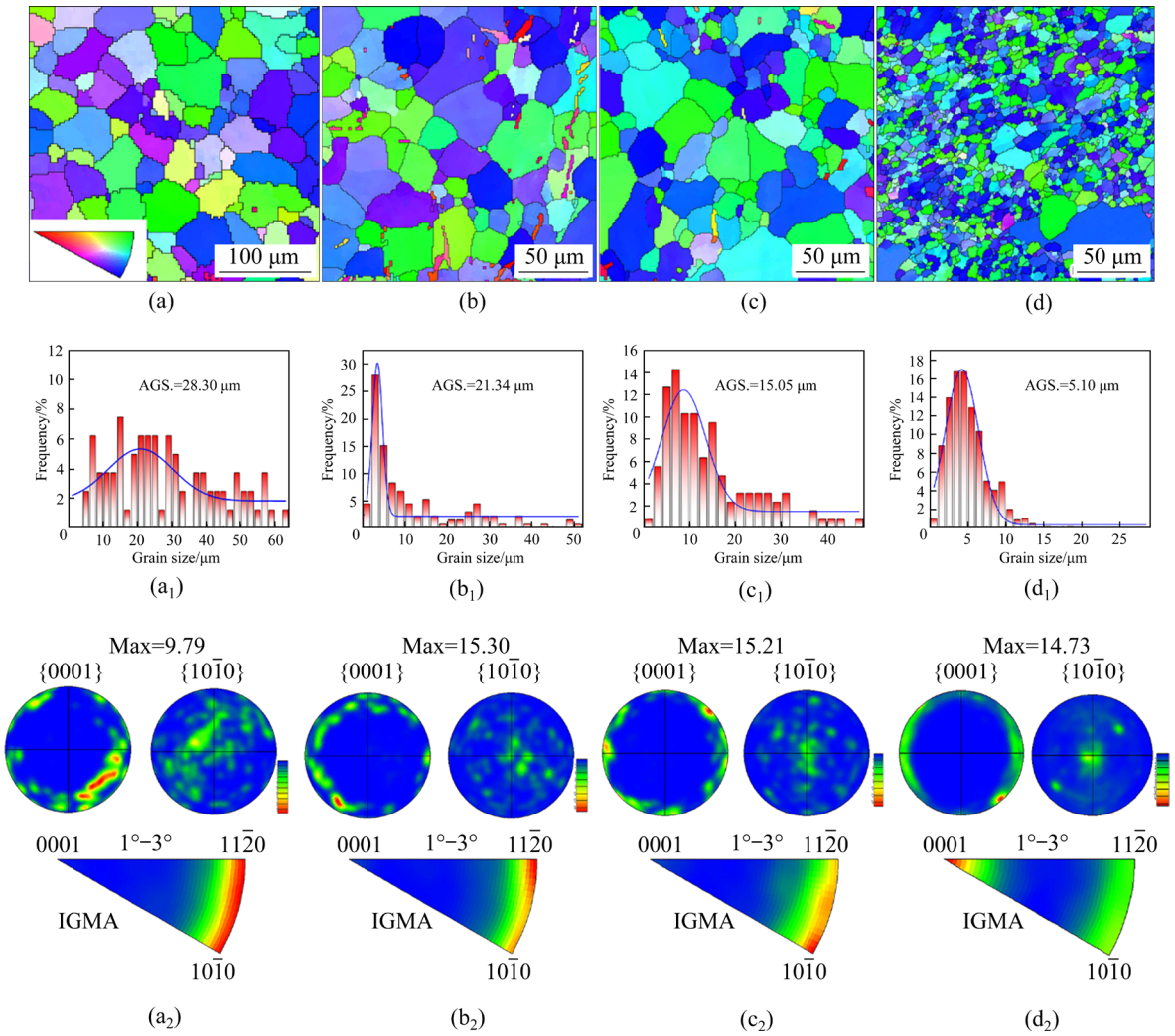

Fig. 5 EBSD micrographs (a−d), grain size distribution histogram (a_1−d_1), pole figures and IGMA maps (a_2−d_2) of as-extruded Mg−*x*Mn alloys: (a, a_1, a_2) Pure Mg; (b, b_1, b_2) Mg−0.3Mn alloy; (c, c_1, c_2) Mg−0.6Mn alloy; (d, d_1, d_2) Mg−0.9Mn alloy

the IGMA maps from Figs. 5(a_2) to (d_2) show that the distribution of in-grain misorientation is concentrated at $(10\bar{1}0)-(11\bar{2}0)$ axis in pure Mg. However, when the Mn content is 0.9 wt.%, the in-grain misorientation is concentrated at (0001) axis. These results exhibit that the increase of Mn content makes the deformation mode gradually dominated by prismatic slip.

Figure 6 depicts the Schmid factor (SF) distribution and histograms for various slip systems of extruded Mg−*x*Mn alloys. In addition to the SF values of prismatic ⟨*a*⟩ slip, it is found that SF values of basal ⟨*a*⟩ slip and pyramidal slips for all the samples are larger than 0.3, and that of the pyramidal I ⟨*c*+*a*⟩ slip is the largest, about 0.41. It is noteworthy that the SF value of the prismatic ⟨*a*⟩ slip changes significantly with the increase of Mn content, from 0.26 to 0.32. The initiation of the slip system becomes easier as the SF value approaches 0.5 in accordance with the SF law. Furthermore, a large SF value indicates a soft grain orientation. Thus, the increase in Mn content promotes the participation of prismatic ⟨*a*⟩ slip, which matches the IGMA results above.

The TEM results of 10% tensile deformed Mg−0.9wt.%Mn alloy are exhibited in Fig. 7. From Fig. 7(a), it is evident that there are many nano-fine precipitated particles throughout the Mg matrix, and a small number of particles dispersed near grain boundaries. According to the EDS results of Points 1−3 (Fig. 7(b)), nanoparticles are Mn-enriched phases, and nanoparticles are considered as Mn particles, due to the result of EDS and the only precipitation phase in the Mg-rich corner of

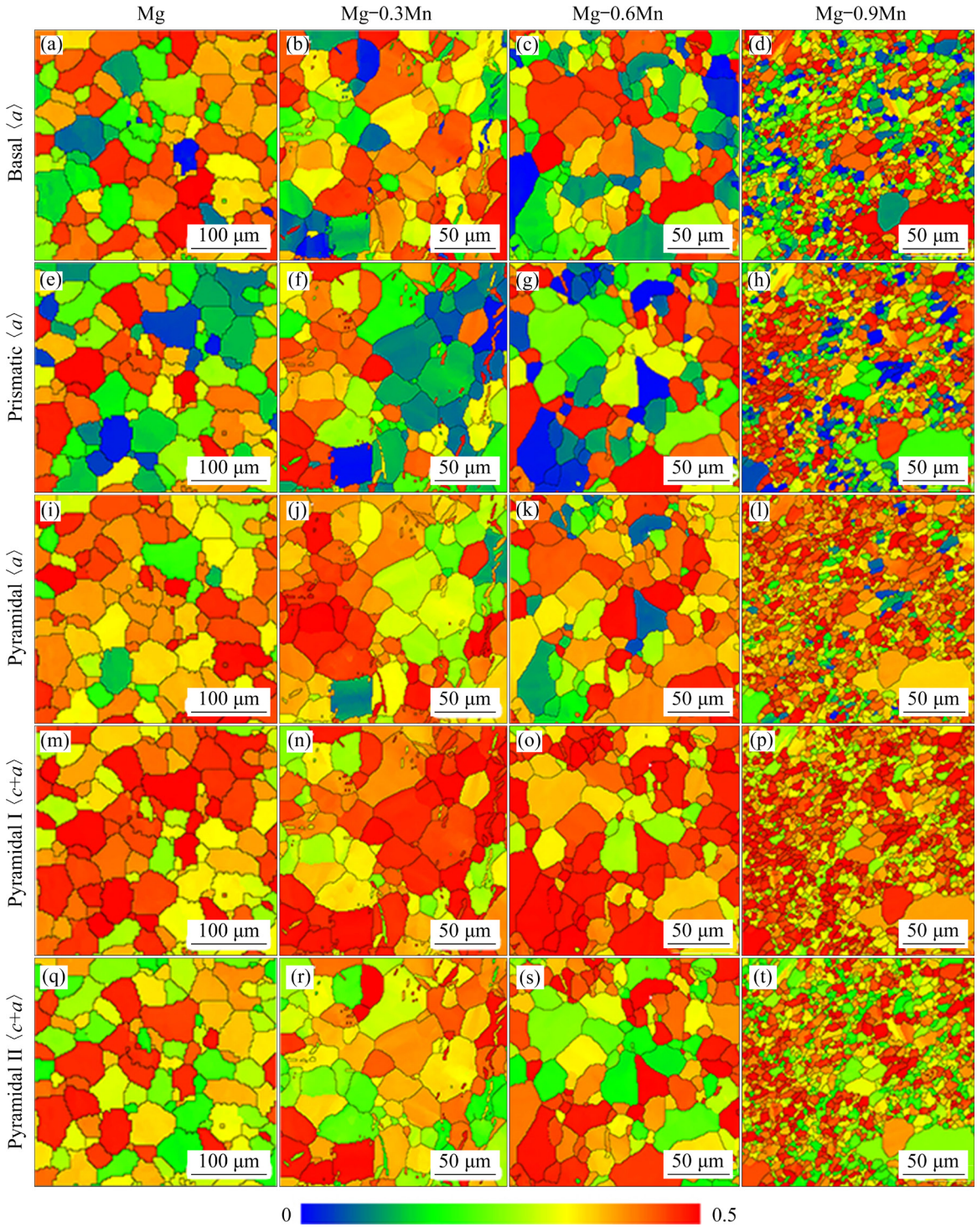

Fig. 6 SF maps for various slip systems of extruded Mg−*x*Mn alloy: (a) 0.34; (b) 0.33; (c) 0.28; (d) 0.26; (e) 0.26; (f) 0.25; (g) 0.28; (h) 0.32; (i) 0.37; (j) 0.37; (k) 0.36; (l) 0.38; (m) 0.40; (n) 0.41; (o) 0.42; (p) 0.41; (q) 0.34; (r) 0.36; (s) 0.36; (t) 0.35

Mg−Mn binary alloys. And Point 2 in Fig. 7(a) shows that parts of Mn are dissolved in the Mg matrix. Additionally, it has been discovered that there are many dislocations in the matrix, where Mn particles exist. Figure 7(d) shows high-resolution transmission electron microscopy (HRTEM) of Mn particles. It can be clearly seen that the precipitated phase is coherent with the matrix, and the orientation between Mn and Mg matrix is $[0001]_{Mg}//[111]_{Mn}$, and $[2\bar{1}\bar{1}0]_{Mg}//[011]_{Mn}$. Moreover, the interplanar spacing of Mn particles is about 0.69 nm.

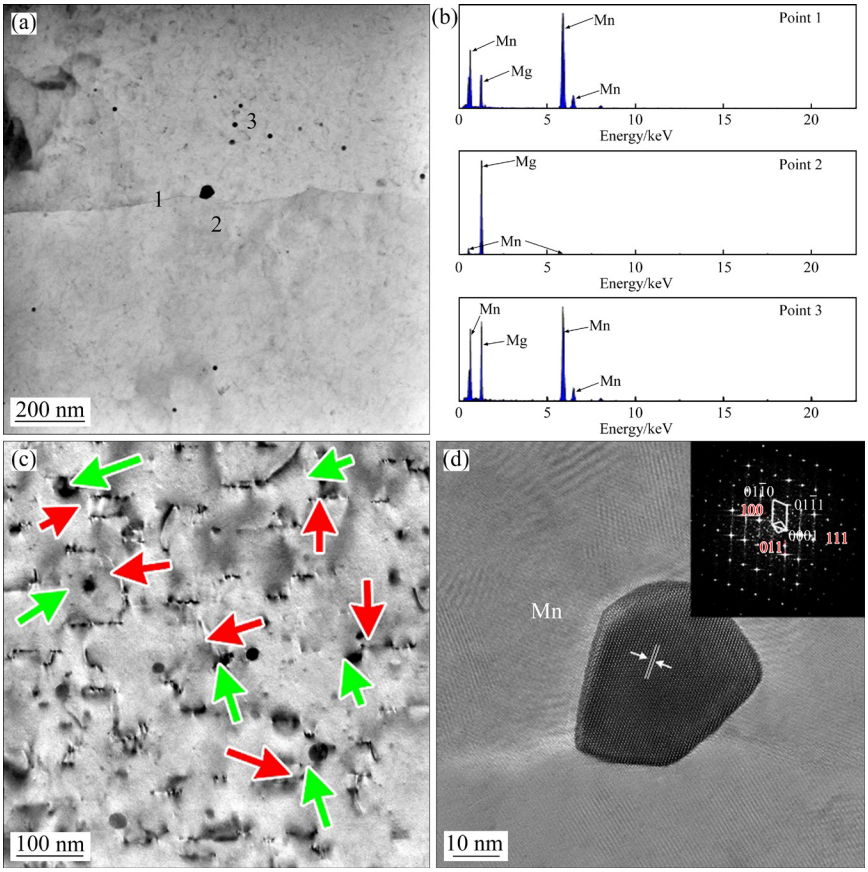

Fig. 7 TEM results of 10% tensile deformed Mg−0.9Mn alloy: (a) Bright-field TEM image; (b) Corresponding EDS result of (a); (c) Bright-field TEM image of dislocations and precipitated particles; (d) HRTEM image of Mn particles

3.4 Work hardening behavior

The work-hardening behavior of as-extruded Mg−*x*Mn alloys is shown in Fig. 8. Figure 8(a) shows the true stress−strain curves, which are converted from the engineering stress−strain curves. The work-hardening behavior can be explained using hardening rate θ [38], hardening capacity H_c [39], and hardening exponent n [40],

$$\theta=\mathrm{d}\sigma/\mathrm{d}\varepsilon \quad (3)$$

$$H_c=(\sigma_{UTS}-\sigma_{0.2})/\sigma_{0.2} \quad (4)$$

$$\sigma=K\varepsilon^n \quad (5)$$

where σ and ε are the true stress and true strain, respectively, and K is the constant. It is evident from Figs. 8(b) and (c) that the work-hardening rate decreases sharply at the beginning, resulting from stage I of the work-hardening short elastic−plastic transition. Besides, all samples do not have a constant strain hardening rate (Stage II) but a dynamic recovery stage (Stage III). θ_{III} represents the work-hardening rate during Stage III, and its value was obtained by extrapolating to $(\sigma-\sigma_{TYS})=0$. Thus, as shown in Fig. 8(c), the values of θ_{III} of pure Mg, Mg−0.3Mn, Mg−0.6Mn, and Mg−0.9Mn alloys are 1752, 2113, 1962, and 1120 MPa, respectively. Besides, from Fig. 8(d), H_c and n decrease from 0.46 and 0.55 to 0.22 and 0.33, respectively. In general, Mn has a weakened effect on the work hardening of pure Mg.

4 Discussion

4.1 Work-hardening behavior with Mn addition

Due to the hcp structure, Mg alloys have different work-hardening behaviors from cubic metals. The work-hardening behavior of Mg alloys is related to the dislocation density and movement during plastic deformation. Thus, the factors influencing the dislocation activities, such as grain size, texture, and solid solubility, need to be studied.

The grain size is an essential factor for the work-hardening behavior of Mg−Mn alloys. From Fig. 8(c), it is found that the slope of these alloys of the work-hardening rate θ vs $(\sigma-\sigma_{0.2})$ in Stage III is almost identical to each other (the dotted line in Fig. 8(c)). The slope of these dot lines represents

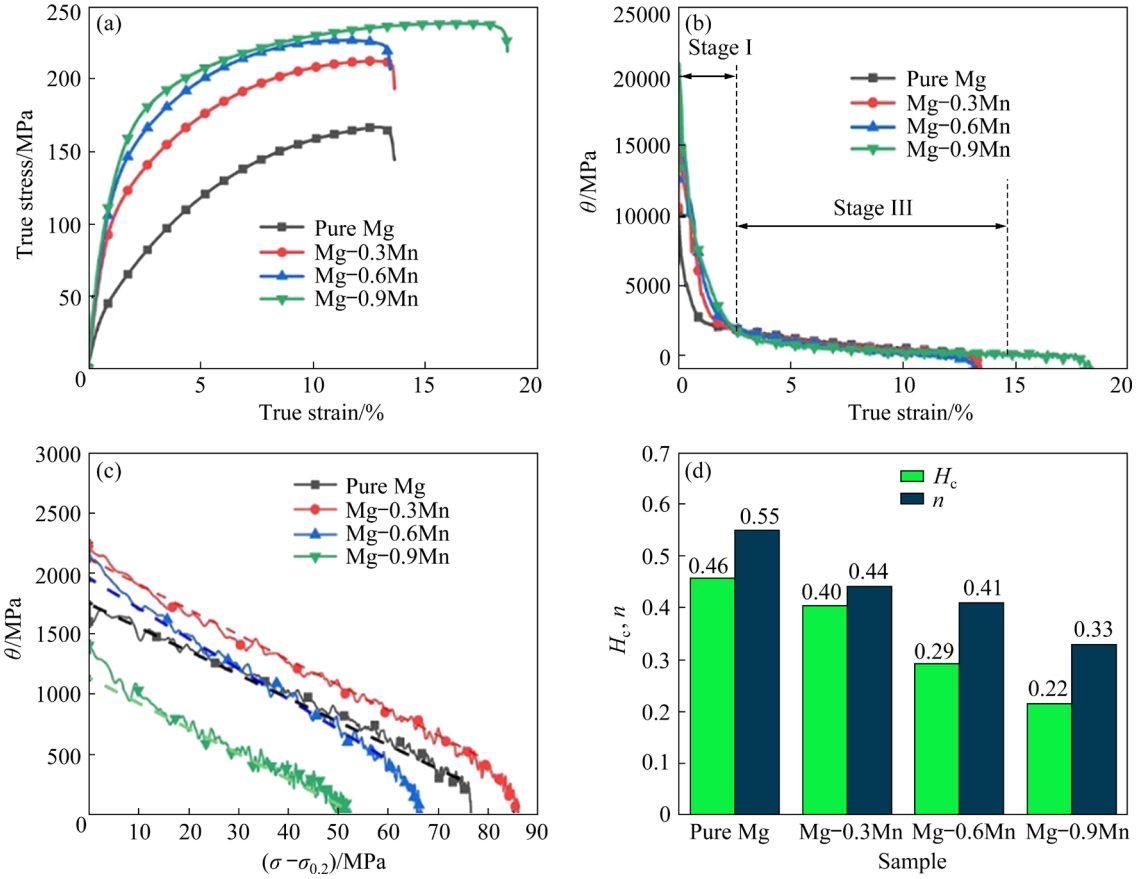

Fig. 8 Work-hardening behavior of as-extruded Mg−*x*Mn alloys: (a) True strain−stress curves; (b) θ vs true strain plots; (c) θ vs ($\sigma-\sigma_{0.2}$) plots; (d) H_c and n plots

the dynamic recovery, and the same slope of these dot lines indicates that the dynamic recovery is not related to the grain size [41]. Hence, the effect of grain size on work-hardening behavior can be explained by the Kock's work-hardening [42]:

$$\frac{\mathrm{d}\rho}{\mathrm{d}\gamma}=k+k_1\rho^{1/2}-k_2\rho \tag{9}$$

$$k=(bd)^{-1} \tag{10}$$

$$\theta=\frac{\mathrm{d}\tau}{\mathrm{d}\gamma}=\frac{\alpha\mu b}{2\rho^{1/2}}\frac{\mathrm{d}\rho}{\mathrm{d}\gamma} \tag{11}$$

where ρ, b, and d are the dislocation density, component of Burger vector, and grain size, respectively; $k_1\rho^{1/2}$ and $k_2\rho$ represent the statistical storage of dislocation and dynamic recovery, respectively. Owing to the dislocation density, dislocation storage rate, and the relationship between ($\mathrm{d}\rho/\mathrm{d}\gamma$) and $\rho^{1/2}$ can be obtained by the $(\sigma-\sigma_{0.2})\theta$ and ($\sigma-\sigma_{0.2}$) curves (Fig. 9). The curves first rise rapidly, which can be fitted with the straight lines. And these lines have different slopes, indicating that the grain size has a significant impact.

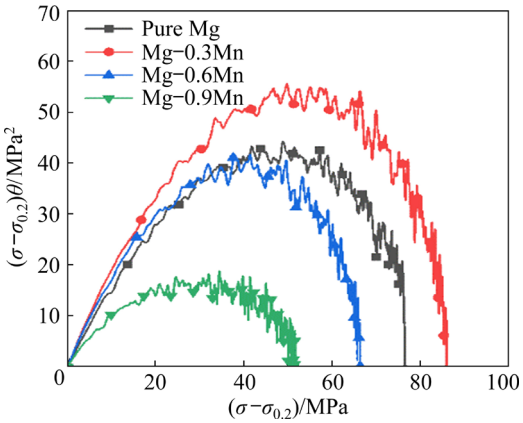

Fig. 9 Relationship between $(\sigma-\sigma_{0.2})\theta$ and ($\sigma-\sigma_{0.2}$) for as-extruded Mg−*x*Mn alloys

According to the results mentioned above, the Mg−0.9Mn alloy has the smallest grain size and the least slope of straightness (Fig. 9). It can be seen that the experimental with the smallest grain size has the lowest work hardening rate. It is known that when the grain size decreases, the grain boundary volume increases, leading to many dislocations accumulating at the grain boundaries during the plastic deformation process and forming a

dislocation concentration zone. Except that, these dislocations can absorb each other to form a large number of low-angle grain boundaries, such as the pink grain boundaries seen in Fig. 10. Consequently, the density of dislocations reduces, resulting in a low work-hardening rate.

Secondly, the texture of alloys also affects the work-hardening behavior. Previous works [43,44] indicated that the texture intensity is related to the Schmid factors for basal and non-basal slips. As indicated before, the SF value of prismatic varies from 0.26 to 0.32, and that of basal slip decreases from 0.34 to 0.26. And the SF value of pyramidal slip is almost unchanged. According to the SF law, the activation of prismatic slip increases during plastic deformation. From above, texture intensity increases from 9.79 to 14.73, with Mn content increasing from 0 to 0.9 wt.%. The results indicate that the orientation of the grain is not favorable for the initiation of basal slip and twinning. Similarly, it is also found that the volume of twins decreases from 18.02% to 1.57% with the increase of Mn content, as shown in Figs. 10(a_1) to (d_1). In addition, the IGMA results also indicate that prismatic slip is also the primary deformation mechanism during tensile deformation. Finally, solid solubility is also an important factor. In this work, since the content of Mn is very low, it will not be discussed in detail.

4.2 Plasticity deformation mechanism with Mn addition

As mentioned above, although the volume fraction of twins decreases with the increase of Mn content, the plasticity of Mg−Mn alloy does not decrease. So, there are other slip systems that coordinate the *c*-axis strain. To get a deeper understanding of the plastic deformation mechanism of Mg−Mn alloy, the slip traces method was applied to illustrating the volume fraction of different slips, as shown in Fig. 11. The results show that basal ⟨*a*⟩ slip is the main deformation mode during the tensile deformation of Mg−*x*Mn alloys. With the Mn addition to 0.9 wt.%, the volume fraction of basal ⟨*a*⟩ slip decreases from 64% to 53%. And the volume fraction of non-basal slip increases from 36% to 47%. Significantly, the volume fraction of pyramidal slip increases from 27% to 38%. The activation of non-basal slip can provide more slip systems to accommodate *c*-axis strain and satisfy the Von-Mises criterion for plasticity deformation. Consequently, the plasticity of Mg−Mn alloys is improved compared with pure Mg.

On the other hand, to explain the involvement of non-basal slip in plastic deformation, two-beam TEM experiments were conducted. The corresponding $g \cdot b=0$ analysis for the two types of

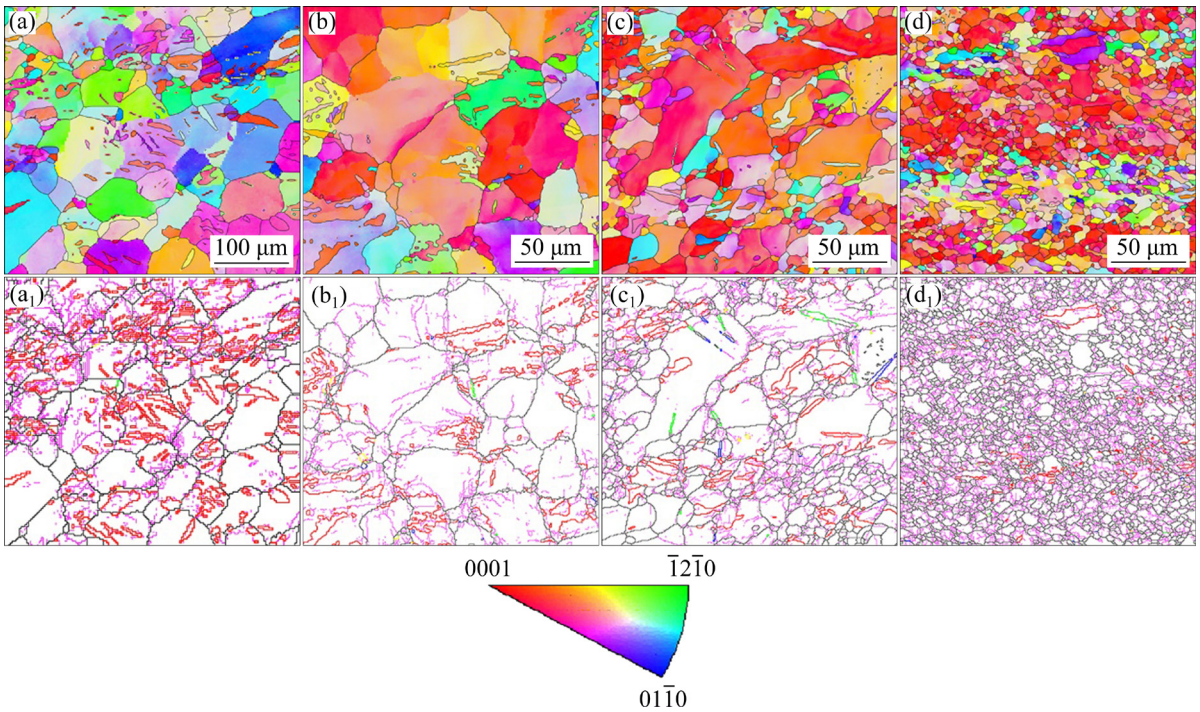

Fig. 10 EBSD micrographs and twins maps of Mg−*x*Mn alloys after being deformed with strain of 5% along ED: (a, a_1) Pure Mg; (b, b_1) Mg−0.3Mn alloy; (c, c_1) Mg−0.6Mn alloy; (d, d_1) Mg−0.9Mn alloy

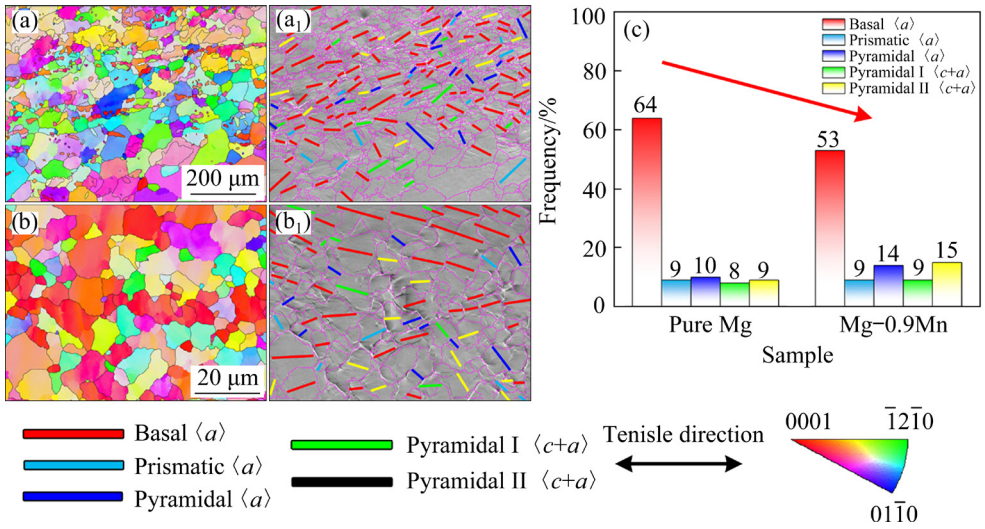

Fig. 11 Orientation maps of as-extruded Mg−*x*Mn alloys and distribution of different slip activity: (a, a_1) Pure Mg; (b, b_1) Mg−0.9Mn; (c) Statistics of identified slip activity

Burgers vector component in Mg−0.9Mn alloy, ⟨*a*⟩ and ⟨*c*+*a*⟩, as well as the three selected *g* of [0002], $[10\bar{1}0]$, and $[10\bar{1}1]$ applied in this study. According to *g*·*b* criterion, ⟨*a*⟩ dislocations are invisible for *g*=[0002] and ⟨*c*+*a*⟩ dislocations are visible. For $g=[10\bar{1}0]$ and $[10\bar{1}1]$, ⟨*a*⟩ dislocation is invisible at $b=[\bar{2}110]$. While $b=[2\bar{1}1\bar{3}]$ and $[2\bar{1}1\bar{3}]$, the ⟨*c*+*a*⟩ dislocations are invisible for $g=[10\bar{1}0]$, and $b=[11\bar{2}\bar{3}]$, $[11\bar{2}\bar{3}]$ and $[\bar{1}2\bar{1}\bar{3}]$, the ⟨*c*+*a*⟩ dislocations are invisible for $g=[10\bar{1}1]$. Thus, the three selected *g* can clearly determine the ⟨*a*⟩ and ⟨*c*+*a*⟩ dislocations in as-extruded Mg−0.9Mn alloy. It has been known that there are many ⟨*c*+*a*⟩ dislocations in Mg−0.9Mn alloy, as shown by the red arrows in Figs. 12(a_1) to (c_1). In addition, as indicated by the yellow and blue arrows, a large number of ⟨*a*⟩ and ⟨*c*⟩ dislocations are also in the Mg−0.9Mn alloy. Therefore, according to the results of TEM, Mn can activate non-basal slip during the plastic deformation.

Polycrystalline plasticity simulations based on the VPSC model were performed on pure Mg and Mg−0.9Mn alloy to further understand the mechanism during plastic deformation. Table 3 exhibits the VPSC simulation parameters of Mg−*x*Mn alloys for different deformation modes. And the simulation results are shown in Fig. 13. Apparently, the predicted true stress−strain curves are consistent with the experimental results.

The deformation mode has been changed from the VPSC results with Mn addition. In the early stage of deformation, basal ⟨*a*⟩ slip is the dominant mode for pure Mg. With the increase of strain, the proportion of basal ⟨*a*⟩ slip decreases gradually, while that of tensile twins increases first and then decreases. Moreover, the proportion of prismatic ⟨*a*⟩ slip increases during the whole plastic deformation. The final volumes of basal ⟨*a*⟩ slip and prismatic ⟨*a*⟩ slip are 80% and 20%, respectively. After adding Mn, basal ⟨*a*⟩ slip is still the dominant slip system in the initial plastic deformation stage. Some prismatic ⟨*a*⟩ slip and pyramidal ⟨*c*+*a*⟩ slip also participate in the process. With the increase of strain, the proportion of basal ⟨*a*⟩ slip decreases

Table 3 VPSC simulation parameters of Mg−*x*Mn alloys for all deformation modes at room temperature

Alloy	Deform mode	τ_0/MPa	τ_1/MPa	θ_0	θ_1
Pure Mg	Basal ⟨*a*⟩ slip	13	25	85	12
	Prismatic ⟨*a*⟩ slip	120	21	60	10
	Pyramidal ⟨*c*+*a*⟩ slip	185	20	6	5
	Tensile twin	75	70	100	0
	Compression twin	300	100	150	0
Mg−0.9Mn	Basal ⟨*a*⟩ slip	20	50	80	30
	Prismatic ⟨*a*⟩ slip	128	30	200	10
	Pyramidal ⟨*c*+*a*⟩ slip	135	10	100	5
	Tensile twin	80	70	100	0
	Compression twin	300	100	150	0

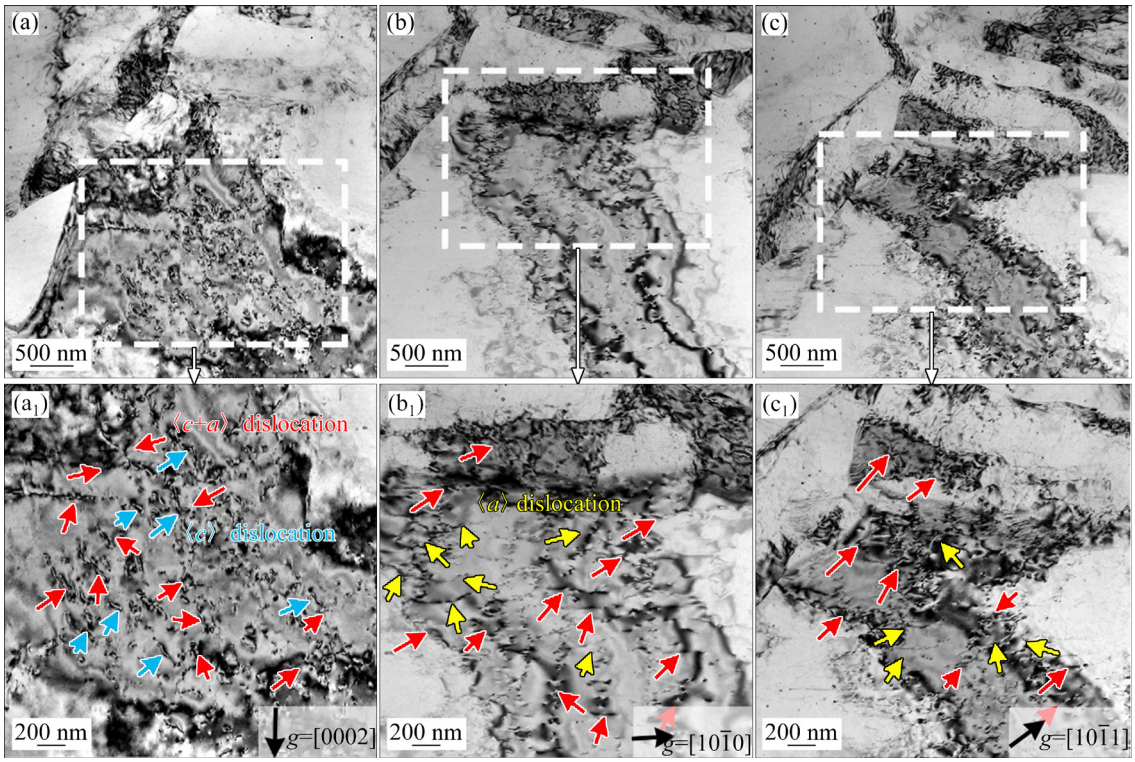

Fig. 12 Transmission electron microscope images for Mg−0.9Mn alloy with elongation of 10% under various operation vectors: (a, a_1) g=[0002]; (b, b_1) g=[10$\bar{1}$0]; (c, c_1) g=[10$\bar{1}$1]

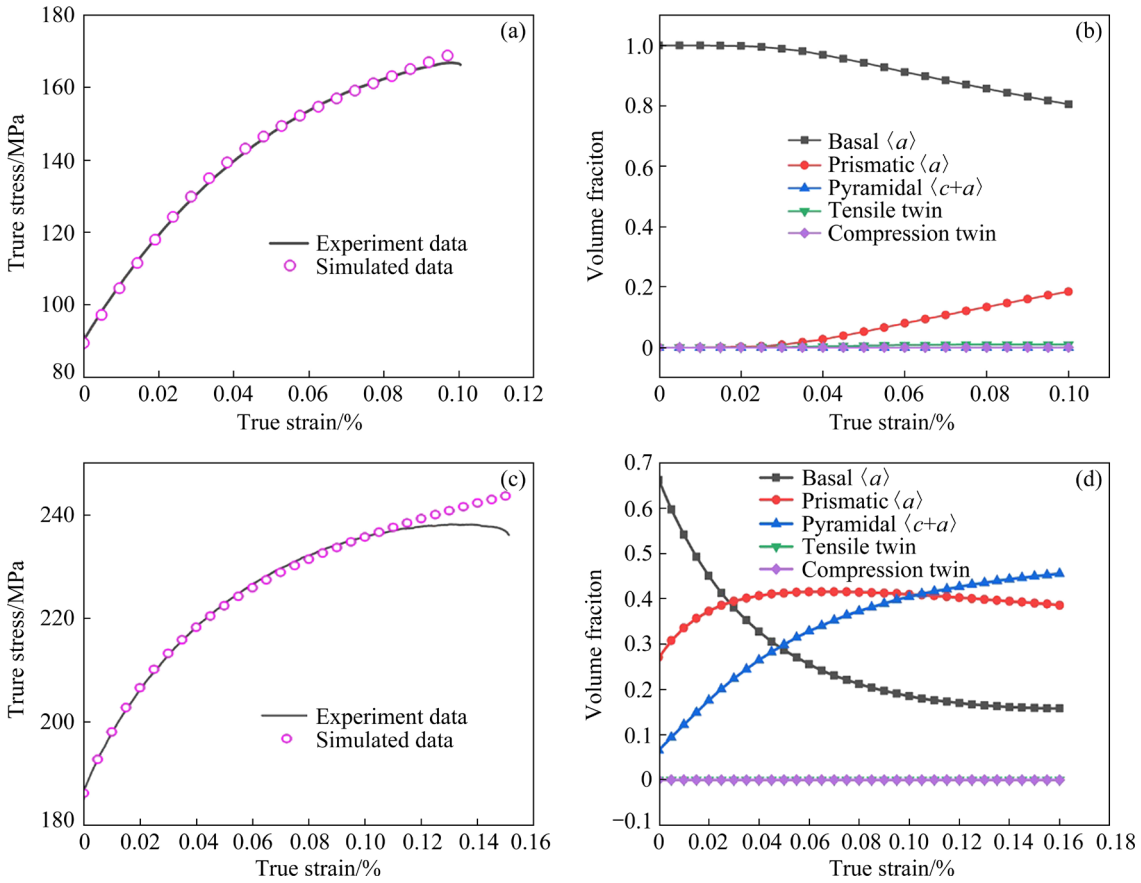

Fig. 13 VPSC simulation results of as-extruded Mg−xMn alloys: (a, b) Pure Mg alloys; (c, d) Mg−0.9Mn alloy

gradually in Mg−0.9Mn alloy, while that of prismatic ⟨*a*⟩ slip increases first and then remains unchanged with strain. It is worth noting that with the further increase of strain, the proportion of pyramidal ⟨*c*+*a*⟩ slip and prismatic ⟨*a*⟩ slip gradually increases to about 46% and 38%, while that of basal ⟨*a*⟩ slip accounts for about 16%. Therefore, pyramidal ⟨*c*+*a*⟩ slip and prismatic ⟨*a*⟩ are the main slip modes in the late deformation stage.

The above results, including the trace analysis, TEM, and VPSC simulation, indicate that the activation of non-basal slip increases with increasing Mn content. The increase in non-basal slip is mainly due to the change in the CRSS gap ($\Delta\tau_0$) between basal slip and non-basal slip. According to the simulation parameters of VPSC, when the Mn content increases from 0 to 0.9 wt.%, the $\Delta\tau_0$ between basal ⟨*a*⟩ and prismatic ⟨*a*⟩ slip increases from 107 to 108 MPa, and $\Delta\tau_0$ between basal ⟨*a*⟩ and pyramidal ⟨*c*+*a*⟩ slip decreases from 172 to 115 MPa. These results show that Mn can reduce $\Delta\tau_0$ between basal ⟨*a*⟩ and pyramidal ⟨*c*+*a*⟩ slip, which makes it easier to activate pyramidal slip. Therefore, the ductility of the Mg−0.9Mn alloy is improved.

5 Conclusions

(1) The average grain size of as-extruded Mg−*x*Mn alloy decreases obviously from 28.30 to 5.10 μm. The maximum texture intensity increases from 9.79 to 14.73. The tensile yield strength of Mg−0.9Mn alloy increases to 180 MPa ,and the elongation increases to 20.31%, compared with pure Mg.

(2) The addition of Mn leads to an obvious reduction in the strain hardening of as-extruded Mg−*x*Mn alloys, showing positive proportional correction with their grain size. With the increase of Mn content from 0 to 0.9 wt.%, the strain hardening capacity and strain hardening exponent decrease from 0.46 to 0.22 and 0.55 to 0.23, respectively.

(3) Mn enhances the activation of pyramidal ⟨*c*+*a*⟩ slip by decreasing the CRSS difference between basal and non-basal slip. Non-basal slip is the main deformation mode during the deformation of Mg−0.9Mn alloy, especially prismatic ⟨*a*⟩ and pyramidal ⟨*c*+*a*⟩ slip. The ductility of Mg alloys with 0.9 wt.% Mn is improved significantly at room temperature.

CRediT authorship contribution statement

Shi-bo ZHOU: Conceptualization, Methodology, Software, Formal analysis, Investigation, Data curation, Writing − Original draft preparation; **Ting-ting LIU:** Conceptualization, Formal analysis, Resources, Supervision, Funding acquisition; **Ai-tao TANG:** Methodology, Validation, Investigation, Resources, Supervision, Funding acquisition; **Hui SHI:** Writing − Review & editing; **Xue-rui JING:** Writing − Review & editing; **Peng PENG:** Methodology, Validation, Formal analysis, Investigation, Writing − Review & editing; **Jian-yue ZHANG:** Writing − Review & editing; **Fu-sheng PAN:** Validation, Resources, Supervision, Funding acquisition.

Declaration of competing interest

The authors declare that they have no known competing financial interests or personal relationships that could have appeared to influence the work reported in this paper.

Acknowledgments

This research was funded by the National Natural Science Foundation of China (Nos. 02110023210043, 51971042, U2167213, 51901028). The authors would like to thank joint lab for electron microscopy of Chongqing University. This work was supported by Sinoma Institute of Materials Research (Guang ZHOU) Co., Ltd (SIMR). The China Scholarship Council is also gratefully acknowledged for financial support for Shi-bo ZHOU (No. 202106050089).

References

[1] WU Guo-hua, WANG Cun-long, SUN Ming, DING Wen-jiang. Recent developments and applications on high-performance cast magnesium rare-earth alloys [J]. Journal of Magnesium and Alloys, 2021, 9: 1−20.

[2] LIU Ting-ting, YANG Qing-shan, GUO Ning, LU Yun, SONG Bo. Stability of twins in Mg alloys – A short review [J]. Journal of Magnesium and Alloys, 2020, 8: 66−77.

[3] YAMAGISHI K, OGAWA Y, ANDO D, SUTOU Y, KOIKE J. Room temperature superelasticity in a lightweight shape memory Mg alloy [J]. Scripta Materialia, 2019, 168: 114−118.

[4] WANG Xue-zhao, WANG You-qiang, NI Chen-bing, FANG Yu-xin, YU Xiao, ZHANG Ping. Effect of Gd content on microstructure and dynamic mechanical properties of solution-treated Mg−*x*Gd−3Y−0.5Zr alloy [J]. Transactions of Nonferrous Metals Society of China, 2022, 32, 2177−2189.

[5] JOOST W J, KRAJEWSKI P E. Towards magnesium alloys for high-volume automotive applications [J]. Scripta Materialia, 2017, 128: 107−112.

[6] SUN Yue-hua, WANG Ri-chu; PENG Chao-qun; WANG Xiao-feng. Effect of Gd on microstructure, mechanical properties, and corrosion behavior of as-homogenized Mg−8Li−3Al−2Zn−0.2Zr alloy [J]. Transactions of Nonferrous Metals Society of China, 2022, 32: 2494−2509.

[7] CHANG Li-li, GUO Jing, SU Xiao-jing. Effect of Y on microstructure evolution and mechanical properties of Mg−4Li−3Al alloys [J]. Transactions of Nonferrous Metals Society of China, 2021, 31: 3691−3702.

[8] YANG Biao-biao, SHI Chen-ying, YE Xian-jue, TENG Jian-wei, LAI Rui-lin, CUI Yu-jie, GUAN Di-kai, CUI Hong-wei, LI Yun-ping, CHIBA A. Underlying slip/twinning activities of Mg−*x*Gd alloys investigated by modified lattice rotation analysis [J]. Journal of Magnesium and Alloys, 2023(3): 998−1015.

[9] LIU Chun-quan, CHEN Xian-hua, ZHANG Wei, ZHANG Yu-sheng, PAN Fu-sheng. Microstructure, creep behavior and corrosion resistance in the ultrafine-grained surface layer of Mg−6Zn−0.2Y−0.4Ce−0.5Zr alloy processed by surfacing friction treatment [J]. Materials Science and Engineering: A, 2020, 776: 138995.

[10] AKHTAR A, TEGHTSOONIAN E. Solid solution strengthening of magnesium single crystals—I Alloying behaviour in basal slip [J]. Acta Metallurgica, 1969, 17: 1339−1349.

[11] AKHTAR A, TEGHTSOONIAN E. Solid solution strengthening of magnesium single crystals—II The effect of solute on the ease of prismatic slip [J]. Acta Metallurgica, 1969, 17: 1351−1356.

[12] CHAPUIS A, DRIVER J H. Temperature dependency of slip and twinning in plane strain compressed magnesium single crystals [J]. Acta Materialia, 2011, 59: 1986−1994.

[13] XIA Nan, WANG Cheng, GAO Yi-peng, HUA Zhen-ming, MA Chen-yi, DU Chun-feng, ZHANG Hang, ZHANG Hong-min, LI Mei-xuan, ZHA Min, WANG Hui-yuan. Enhanced ductility of Mg−1Zn−0.2Zr alloy with dilute Ca addition achieved by activation of non-basal slip and twinning [J]. Materials Science and Engineering: A, 2021, 813: 141128.

[14] ZHAO Jun, JIANG Bin, YUAN Yuan, TANG Ai-tao, SHENG Hao-ran, YANG Tian-hao, HUANG Guang-sheng, ZHANG Ding-fei, PAN Fu-sheng. Influence of Zn addition on the microstructure, tensile properties and work-hardening behavior of Mg−1Gd alloy [J]. Materials Science and Engineering: A, 2020, 772: 138779.

[15] FAN Wen-xue, BAI Yu, LI Guang-yang, CHANG Xing-yang, HAO Hai. Enhanced mechanical properties and formability of hot-rolled Mg−Zn−Mn alloy by Ca and Sm alloying [J]. Transactions of Nonferrous Metals Society of China, 2022, 32: 1119−1132.

[16] JORGEA V D, CARRENO F, RUANO O A. Influence of texture and grain size on work hardening and ductility in magnesium-based alloys processed by ECAP and rolling [J]. Acta Materialia, 2006, 54: 4247−4259.

[17] YAO Yi, LIU Chu-ming, GAO Yong-hao, YU Shi-lun, JIANG Shu-nong, CHEN Zhi-yong. Annealing-induced microstructural evolution and mechanical anisotropy improvement of the Mg−Gd−Y−Zr alloy processed by hot ring rolling [J]. Materials Characterization, 2018, 144: 641−651.

[18] WANG Qing-hang, JIANG Bin, TANG Ai-tao, HE Chao, ZHANG Ding-fei, SONG Jiang-feng, YANG Tian-hao, HUANG Guang-sheng, PAN Fu-sheng. Formation of the elliptical texture and its effect on the mechanical properties and stretch formability of dilute Mg−Sn−Y sheet by Zn addition [J]. Materials Science and Engineering: A, 2019, 746: 259−275.

[19] WANG Qing-hang, LIU Lin-tao, JIANG Bin, FU Jie, TANG Ai-tao, JIANG Zhong-tao, SHENG Hao-ran, ZHANG Ding-fei, HUANG Guang-sheng, PAN Fu-sheng. Twin nucleation, twin growth and their effects on annealing strengths of Mg−Al−Zn−Mn sheets experienced different pre-compressive strains [J]. Journal of Alloys and Compounds, 2020, 815: 152310.

[20] HIDETOSHI S, AIOK S, TOSHIJI M, TADANOBU I. Effect of alloying elements on room temperature tensile ductility in magnesium alloys [J]. Philosophical Magazine, 2016, 96: 2671−2685.

[21] ZHAO De-xin, MA Xiao-long, SRIVASTAVA A, TURNER G, KARAMAN I, XIE K Y. Significant disparity of non-basal dislocation activities in hot-rolled highly-textured Mg and Mg−3Al−1Zn alloy under tension [J]. Acta Materialia, 2021, 207: 116691.

[22] SANDLÖBES S, ZAEFFERER S, SCHESTAKOW I, YI Sang-bong, GONZALEZ-MARTINEZ R. On the role of non-basal deformation mechanisms for the ductility of Mg and Mg−Y alloys [J]. Acta Materialia, 2011, 59: 429−439.

[23] WU Zhao-xuan, AHMAD R, YIN Bing-lun, SANDLÖBES S, CURTIN W A. Mechanistic origin and prediction of enhanced ductility in magnesium alloys [J]. Science, 2018, 359: 447−452.

[24] ZHU Gao-ming, WANG Le-yun, ZHOU Hao, WANG Jin-hui, SHEN Yao, TU Peng, ZHU Hong, LIU Wei, JIN Pei-peng, ZENG Xiao-qin. Improving ductility of a Mg alloy via non-basal slip induced by Ca addition [J]. International Journal of Plasticity, 2019, 120: 164−179.

[25] ZENG Zhuo-ran, BIAN Ming-zhe, XU Shi-wei, DAVIES C H J, BIRBILIS N, NIE Jian-feng. Effects of dilute additions of Zn and Ca on ductility of magnesium alloy sheet [J]. Materials Science and Engineering: A, 2016, 674: 459−471.

[26] YU Zheng-wen, TANG Ai-tao, HE Jie-jun, GAO Zheng-yuan, SHE Jia, LIU Jian-guo, PAN Fu-sheng. Effect of high content of manganese on microstructure, texture and mechanical properties of magnesium alloy [J]. Materials Characterization, 2018, 136: 310−317.

[27] ZHOU Shi-bo, PENG Peng, ZHANG Jian-yue, LIU Ting-ting, PAN Fu-sheng. Study on the effects of manganese on the grain structure and mechanical properties of Mg−0.5Ce alloy [J]. Materials Science and Engineering: A, 2021, 821: 141567.

[28] YU Zheng-wen, HU Meng-die, TANG Ai-tao, WU Ming-song, HE Jie-jun, GAO Zheng-yuan, WANG Fang-yuan, LI Cai-yu, CHEN Bin, LIU Jian-guo. Effect of aluminium on the microstructure and mechanical properties of as-cast magnesium–manganese alloys [J]. Materials Science and Technology, 2017, 33: 2086−2096.

[29] SOMEKAWA H, BASHA D A, SINGH A. Deformation

behavior at room temperature ranges of fine-grained Mg−Mn system alloys [J]. Materials Science and Engineering: A, 2019, 766: 138384.
[30] PENG Peng, SHE Jia, TANG Ai-tao, ZHANG Jian-yue, SONG Kai, YANG Qing-shan, PAN Fu-sheng. A strategy to regulate the microstructure and properties of Mg−2.0Zn−1.5Mn magnesium alloy by tracing the existence of Mn element [J]. Journal of Alloys and Compounds, 2022, 890: 161789.
[31] BIELER T R, EISENLOHR P, ROTERS F, KUMAR D, MASON D E, CRIMP M A, RAABE D. The role of heterogeneous deformation on damage nucleation at grain boundaries in single phase metals [J]. International Journal of Plasticity, 2009, 25: 1655−1683.
[32] SUH B C, KIM J H, BAE J H, HWANG J H, SHIM M S, KIM N J. Effect of Sn addition on the microstructure and deformation behavior of Mg−3Al alloy [J]. Acta Materialia, 2017, 124: 268−279.
[33] GUO Xiao-qian, CHAPUIS A, WU Pei-dong, LIU Qing, MAO Xian-biao. Experimental and numerical investigation of anisotropic and twinning behavior in Mg alloy under uniaxial tension [J]. Materials & Design, 2016, 98: 333−343.
[34] AGNEW S R, YOO M H, TOMÉ C N. Application of texture simulation to understanding mechanical behavior of Mg and solid solution alloys containing Li or Y [J]. Acta Materialia, 2001, 49: 4277−4289.
[35] MA Quan-cang, EL KADIRI H, OPPEDAL A L, BAIRD J C, LI Bin, HORSTEMEYER M F, VOGEL S C. Twinning effects in a rod-textured AM30 Magnesium alloy [J]. International Journal of Plasticity, 2012, 29: 60−76.
[36] GUO Ting-ting, SISKA F, BARNETT M R. Distinguishing between slip and twinning events during nanoindentation of magnesium alloy AZ31 [J]. Scripta Materialia, 2016, 110: 10−13.
[37] GUO Ting-ting, SISKA F, CHENG Jun, BARNETT M. Initiation of basal slip and tensile twinning in magnesium alloys during nanoindentation [J]. Journal of Alloys and Compounds, 2018, 731: 620−630.
[38] KOCKS U F, MECKING H. Physics and phenomenology of strain hardening: The FCC case [J]. Progress in Materials Science, 2003, 48: 171−273.
[39] LIU Ting-ting, PAN Fu-sheng, ZHANG Xi-yan. Effect of Sc addition on the work-hardening behavior of ZK60 magnesium alloy [J]. Materials & Design, 2013, 43: 572−577.
[40] ZHAO Chao-yue, CHEN Xian-hua, PAN Fu-sheng, GAO Shang-yu, ZHAO Di, LIU Xiao-fang. Effect of Sn content on strain hardening behavior of as-extruded Mg−Sn alloys [J]. Materials Science and Engineering: A, 2018, 713: 244−252.
[41] AGNEW S R, TOMÉ C N, BROWN D W, HOLDEN T M, VOGEL S C. Study of slip mechanisms in a magnesium alloy by neutron diffraction and modeling [J]. Scripta Materialia, 2003, 48: 1003−1008.
[42] LI Qi, HUANG Guang-jie, HUANG Xin-de, PAN Shi-wei, TAN Chao-lan, LIU Qing. On the texture evolution of Mg−Zn−Ca alloy with different hot rolling paths [J]. Journal of Magnesium and Alloys, 2017, 5: 166−172.
[43] ZHAO Chao-yue, LI Zi-yan, SHI Jia-hui, CHEN Xian-hua, TU Teng, LUO Zhu, CHENG Ren-ju, ATRENS ANDREJ, PAN Fu-sheng. Strain hardening behavior of Mg−Y alloys after extrusion process [J]. Journal of Magnesium and Alloys, 2019, 7: 672−680.
[44] ZHAO Chao-yue, CHEN Xian-hua, PAN Fu-sheng, WANG Jing-feng, GAO Shang-yu, TU Teng, LIU Chun-quan, YAO Jia-hao, ATRENS A. Strain hardening of as-extruded Mg−*x*Zn (*x*=1, 2, 3 and 4 wt.%) alloys [J]. Journal of Materials Science & Technology, 2019, 35: 142−150.

通过添加微量 Mn 元素激活非基面滑移提高镁合金塑性

周世博[1,2]，刘婷婷[3]，汤爱涛[1,4]，时 慧[2]，敬学锐[1]，彭 鹏[5]，章建跃[6]，潘复生[1,4]

1. 重庆大学 材料科学与工程学院，重庆 400044；
2. Institute of Metallic Biomaterials, Helmholtz-Zentrum Hereon, Max-Planck-Straße 1, D-21502, Geesthacht, Germany；
3. 西南大学 材料与能源学院，重庆 400715；
4. 重庆大学 镁合金国家工程研究中心，重庆 400044；
5. 重庆科技学院 冶金和材料工程学院，重庆 401331；
6. Department of Materials Science and Engineering, The Ohio State University, Columbus, OH 43210, USA

摘 要：分析微量锰添加对镁合金显微组织和力学性能的影响。采用电子背散射技术、迹线分析、透射电镜和粘塑性自洽模拟等方法研究变形过程中的塑性变形机理。结果表明：Mn 的加入使 Mg−Mn 合金的平均晶粒尺寸由 28.30 μm 减小到 5.10 μm；同时，随着 Mn 含量的增加，样品的断裂伸长率由 14.33%提高到 20.33%，屈服强度则由 84 MPa 提高到 180 MPa。这种同时提高塑性和强度的原因是基面滑移和非基面滑移之间的临界剪切应力差从 173 MPa 减小到 115 MPa，导致非基面滑移活动明显增加。通过微合金元素调整滑移系统差异为开发具有高强度和延展性的镁合金提供了一种途径。

关键词：镁合金；显微组织演变；力学性能；塑性；变形机理

(Edited by Xiang-qun LI)